

An investigation into the role of the acid catalyst on the structure and anticorrosion properties of hybrid sol-gel coatings

AUTHOR(S)

Maikki Cullen, Alicja Kaworek, Joseph Mohan, Brendan Duffy, Mohamed Oubaha

CITATION

Cullen, Maikki; Kaworek, Alicja; Mohan, Joseph; Duffy, Brendan; Oubaha, Mohamed (2022): An investigation into the role of the acid catalyst on the structure and anticorrosion properties of hybrid sol-gel coatings. Royal College of Surgeons in Ireland. Journal contribution. <https://hdl.handle.net/10779/rcsi.17933813.v1>

HANDLE

[10779/rcsi.17933813.v1](https://hdl.handle.net/10779/rcsi.17933813.v1)

LICENCE

CC BY-NC-ND 4.0

This work is made available under the above open licence by RCSI and has been printed from <https://repository.rcsi.com>. For more information please contact repository@rcsi.com

URL

[https://repository.rcsi.com/articles/journal_contribution/An_investigation_into_the_role_of_the_acid_catalyst_o
n_the_structure_and_anticorrosion_properties_of_hybrid_sol-gel_coatings/17933813/1](https://repository.rcsi.com/articles/journal_contribution/An_investigation_into_the_role_of_the_acid_catalyst_on_the_structure_and_anticorrosion_properties_of_hybrid_sol-gel_coatings/17933813/1)



An investigation into the Role of the Acid Catalyst on the Structure and Anticorrosion Properties of Hybrid Sol-Gel Coatings

Maikki Cullen^{a,b,c}, Alicja Kaworek^{a,b}, Joseph Mohan^{a,b}, Brendan Duffy^{a,b}, Mohamed Oubaha^{a,b,*}

^a School of Chemical and Pharmaceutical Sciences, Technological University Dublin, City Campus, Kevin Street, Dublin 8, Ireland

^b Centre for Research in Engineering Surface Technology, FOCAS Institute, Technological University Dublin, City Campus, 13 Camden Row, Dublin 8, Ireland

^c Royal College of Surgeons in Ireland - Bahrain, Adliya, Kingdom of Bahrain

ARTICLE INFO

Keywords:

Sol-Gel
Hybrids
Coatings
Hydrolysis
Condensation
Anticorrosion
Structure
Catalyst

ABSTRACT

This paper investigates the role of the acid catalyst on the structure and anticorrosion barrier performances of a dual hybrid sol-gel coating composed 3-trimethoxysilylpropylmethacrylate and a zirconium complex and deposited on AA2024-T3 alloy. Along with the variation of the acid catalyst in the range 0.3 to 2, the zirconium complex concentration in the silicate matrix is altered from 10 to 30%. Mol.

The structure of the materials is characterised using dynamic light scattering, Fourier-transform infrared spectroscopy, and ²⁹Silicon nuclear magnetic resonance spectroscopy, while the thermal behaviour is identified by differential scanning calorimetry and the coating morphology analysed using scanning electron microscopy/energy dispersive x-ray spectroscopy. The anticorrosion barrier properties are characterised by electrochemical impedance spectroscopy and neutral salt spray.

It is shown that the acid catalyst concentration has a direct impact on the kinetics of the hydrolysis and condensation reactions and that those effects can be controlled by the content of zirconium. These individual or combined alterations are found to directly impact the formation of Si-O-Zr bonds, thus the interconnectivity between the silicate matrix and the zirconium complex modifier, resulting in hybrid structures with altered densities. For the materials composed of 10 and 20 % of zirconium complex and when the pH is lowered, the relative concentrations of siloxane bonds is increased at the expenses of the Si-O-Zr bonds. When the concentration of zirconium complex is increased to 30 % and as the pH is increased, a higher competition in the formation of Si-O-Zr bonds takes place and are preferentially formed over the higher condensed Si-O-Si bonds.

The corrosion testing show that the coatings with the highest barrier properties are found when the interconnectivity between the silicate and zirconium complex is maximum, thus for the materials exhibiting the highest condensation degrees.

1. Introduction

The development of eco-friendly coatings for corrosion protection of metallic substrates has seen extensive research in many areas, including Cr(III) based conversion coatings [1,2], phosphate based conversion coatings [3], rare earth metals [4,5], vanadium based conversion coatings [6] and hybrid sol-gel coatings [7–10]. However, hybrid sol-gel materials seem to have a higher focus than those listed above, due to many favourable factors enabling the design of coatings with multifunctional capabilities. There is a wide range of organofunctional alkoxide precursors commercially available that can be employed

individually or in multiple combinations, thus achieving multifunctional materials. In addition to the multifunctional opportunities these materials offer, the sol-gel process enables additional introduction of organic and inorganic network modifiers and additives to control the structure, morphology and surface properties of the materials, thus opening many avenues of research in the wider material science domain and particularly in the field of coatings [11]. The precursors and the preparation conditions can have direct effects on the physicochemical properties of the final coatings, including chemical, physical and mechanical features. Particularly, preparation conditions such as the nature and functionalities of the precursors, the hydrolysis degree and the pH play an

* Corresponding author.

E-mail addresses: mohamed.oubaha@tudublin.ie, am.oubaha@gmail.com (M. Oubaha).

<https://doi.org/10.1016/j.tsf.2021.138703>

Received 23 September 2020; Received in revised form 14 April 2021; Accepted 17 April 2021

Available online 22 April 2021

0040-6090/© 2021 The Author(s).

Published by Elsevier B.V. This is an open access article under the CC BY-NC-ND license

(<http://creativecommons.org/licenses/by-nc-nd/4.0/>).

important role in the condensation of the inorganic network and on the subsequent properties of the prepared materials. For example, for corrosion protection of aluminium alloys, the authors have highlighted in a previous study [12] that the inclusion of a zirconium complex within an organosilane matrix acts as a network densifier and that the content of zirconium plays a critical role on the anticorrosion performances of the coatings when exposed to aggressive alkaline environments. A correlation between the content of zirconium and the density of the network was proposed on the basis of the interactions between the organosilane matrix and the transition metal. A suitable concentration of 20 % of zirconium was found to maximise the condensation of the network while providing the most performing anticorrosion performances. In another study [13], the role of the hydrolysis degree for a fixed acid catalyst concentration was investigated on the structure, morphology and anticorrosion performances of the same formulation. It was found that the degree of hydrolysis had an effect on the interactions between the silane matrix and the transition metal modifier. A compromise between both the hydrolysis degree and concentration of transition metal modifier were essential in producing a highly connected and interpenetrated network between the silicate and zirconate species, which can increase the corrosion resistance of the coatings. It was demonstrated that competition in the formation of Si-O-Si and Si-O-Zr bonds takes place and can be controlled by the degree of hydrolysis and the concentration of the zirconium complex. At a pH value fixed at 1 for the hydrolysis step of the organosilane, an optimum hydrolysis degree of 50 % against the total reactive alkoxide groups was found to maximise the condensation of the inorganic network and anticorrosion performances.

Nevertheless, in light of these studies, it appeared that further investigations are needed to optimise the connectivity between the silicate and zirconate species, thus possibly achieving coatings with improved corrosion resistances. Indeed, by optimising the connectivity of the inorganic network, the density of the coatings may be increased and as direct result an improvement of their barrier properties against corrosion. To tackle this objective, one the critical synthetic parameters to investigate in sol-gel chemistry is the nature of the acid catalyst as it directly governs the kinetics and rate of hydrolysis of the precursors, their condensation processes and their subsequent physicochemical properties. Indeed, the critical impact the catalyst's pH has on the structure and morphology of the materials fabricated through sol-gel chemistry has been widely documented primarily on silane-based precursors [14–16]. Briefly, under acidic conditions the hydrolysis kinetics of the silane is favoured over the condensation that tends to form high density, low pore volume gels. Under basic conditions, the condensation reaction is faster than hydrolysis, resulting in highly condensed species that form densely packed arrays of identifiable particles, around which are large voids. However, so far, no study has highlighted the effect of the pH of the acid catalyst on the structure of dual silane and transition metal sol-gel materials and the subsequent impact this may have on the anticorrosion barrier performances.

Therefore, this paper proposes to highlight the impact of the pH of the acid catalyst on the structure and corrosion resistance of coatings prepared from a well-established hybrid sol-gel material composed of 3-trimethoxysilylpropylmethacrylate and a zirconium complex [12, 13]. As our previous studies showed that the zirconium complex plays a major role in the formation of siloxane and Si-O-Zr bonds, its concentration within the silicate matrix has also been varied to highlight the effect of the pH variation may produce on the reactivity of the zirconium complex in the condensation process of the inorganic species, primarily its interaction with the silicate matrix. The developed materials are characterised in terms of structure using dynamic light scattering (DLS), Fourier-transform infrared spectroscopy (FTIR), ^{29}Si nuclear magnetic resonance spectroscopy (^{29}Si -NMR), and scanning electron microscopy/energy dispersive X-ray spectroscopy (SEM/EDX), the thermal behaviour by differential scanning calorimetry (DSC) and the corrosion resistance by electrochemical impedance spectroscopy (EIS)

and neutral salt spray (NSS). A correlation between the formulation of the materials and their structure and performances is proposed.

2. Materials and Methods

2.1. Sol-Gel Synthesis

The materials were prepared from the combination of an organosilane and a transition metal sol-gel reactive precursor, namely MAPTMS (3-methacryloxypropyltrimethoxysilane, Assay 99 % in methanol, Sigma Aldrich Irl.) and ZPO (zirconium (IV) n-propoxide, Assay 70 % in propanol, Sigma Aldrich Irl.), respectively. Because the precursors have dramatically different reactivities to water, slow for the organosilane and violent for the transition metal that precipitates in the presence of water, a suitable three-step sol-gel process was established to avoid precipitation and enable preparation of stable and transparent sols. MAPTMS is pre-hydrolysed with a nitric acid aqueous solution (HNO_3 , ACS reagent, Sigma Aldrich Irl.). The nitric acid solution is added dropwise for approximately 5 minutes until the solution becomes miscible and then mixed using a stirring plate for 45 min. This provides a theoretical hydrolysis rate of 25 % of the total methoxide groups (see below for the acid concentration). In parallel, ZPO is chelated by MAAH (methacrylic acid, $\text{C}_4\text{H}_6\text{O}_4$, Assay > 98 %, Sigma Aldrich Irl.) in a stoichiometric ratio and mixed using a stirring plate for a duration of 45 min to achieve a zirconium complex where 50 % of the propoxide groups are complexed. The last step of the process consisted of mixing the pre-hydrolysed organosilane and the complexed transition metal together for 5 minutes followed by a hydrolysis employing deionised water to complete hydrolysis to a rate of 50 % against the total alkoxide groups. The obtained sols were found to be fully transparent and particle-free, suggesting the kinetics of hydrolysis and condensation reactions were suitably performed with the established three-step sol-gel process. The difference with the previous studies is that here the concentration of the acid catalyst used in the pre-hydrolysis of the MAPTMS was varied along with the concentration of the transition metal alkoxide precursor, as described in Table 1.

The materials prepared with a 0.1 M HNO_3 (B, E and H) have been reported in a previous study by the authors, where the hydrolysis degree was investigated (denoted E, H and K) and are included in this study in order to accurately compare the materials prepared with other HNO_3 concentrations [10].

2.2. Preparation of Sol-Gel Coatings

The 24-hour aged sol-gels are filtered using a 0.45 μm syringe filter and then spin-coated onto the prepared AA2024-T3 panels (Amari Irl.) at 1000 rpm under an alcohol saturated environment. The aluminium panels were prepared by degreasing with isopropanol and then etched with hydrofluoric acid aqueous solution (Novaclean 104, Henkel, Irl.) and a sulphuric acid aqueous solution (Novox 302, Henkel, Irl.). This final acid rinsing step enabled the surface activation by creation of hydroxyl groups. The preparation of the panels and the coating method

Table 1
Material formulations

Sample name	Sample series	[HNO_3]	pH value	MAPTMS/ZPO/MAAH (mol. %)
A	Series 1	0.01 M	2	90/10/10
B	Series 1	0.10 M	1	90/10/10
C	Series 1	0.50 M	0.3	90/10/10
D	Series 2	0.01 M	2	80/20/20
E	Series 2	0.10 M	1	80/20/20
F	Series 2	0.50 M	0.3	80/20/20
G	Series 3	0.01 M	2	70/30/30
H	Series 3	0.10 M	1	70/30/30
I	Series 3	0.50 M	0.3	70/30/30

allows for the fabrication of highly homogenous and residual-free coatings. The coatings are then stabilised via heat curing at 120°C for 1 hour.

2.3. DLS

The particle size of the sol-gels was determined at ambient temperature using the DLS technique on a Malvern Nano-ZS instrument.

2.4. FTIR

FTIR spectra of the coatings were obtained using a Perkin Elmer GX instrument operating in the ATR mode within the 600 - 4000 cm^{-1} spectral range.

2.5. ^{29}Si -NMR spectroscopy

The ^{29}Si -NMR spectra were recorded on liquid sols at ambient temperature using a 400 MHz Bruker spectrometer. Experimental conditions were as follows: frequency 46.69 MHz, recycle delay 4 s, pulse $\pi/3$ (8 μs), spectral width 500 ppm and 80 scans. The signal chemical shift reference was tetramethylsilane and the FID (free induction decay) processing used a 10 Hz line broadening. Dimethyl sulfoxide was used as the lock solvent.

2.6. DSC

DSC spectra were recorded under an air atmosphere at a heating rate of 5°C/min between 20°C and 200°C using a Shimadzu DSC QC instrument. The samples were prepared by dropping 10 μl of the liquid sol-gels into an aluminium sample pan.

2.7. SEM/EDX

SEM images and EDX analyses were recorded using a Hitachi SU-70 SEM using an accelerating voltage of 5 keV for SEM images and 20 keV for EDX analyses

2.8. EIS

EIS data were recorded using a Solartron SI 1287/1255B system comprising a frequency analyser and a potentiostat. All scans were acquired in the region from -0.4 to +0.5 V vs. Eoc, with a scan rate of 20 mV/s at room temperatures ($20 \pm 2^\circ\text{C}$).

2.9. NSS

NSS testing were complete in a neutral salt spray testing chamber, according to the ISO 9227 standards. The samples were exposed to a salt fog atmosphere generated from 5 wt. % NaCl solution at 35°C (± 1) in an enclosed cabinet. The back and sides of each panel are protected with insulating tape.

The coatings preparation and all characterisation techniques employed herein (DLS, FTIR, ^{29}Si -NMR, DSC, SEM, EIS and NSS) have previously been described in a study by the authors [10].

3. Results and Discussion

3.1. DLS Analysis

Particle sizes for all materials were recorded after 24 hours of ageing and are shown in Fig. 1. The full width at half maximum (FWHM) for each material has been plotted along with its max peak in Fig. 2. In all series the nanoparticles range in sizes from 2–28 nm. It was observed that regardless of the pH of the synthesis that the band extremum remained the same within each series. This shows that the nanoparticle

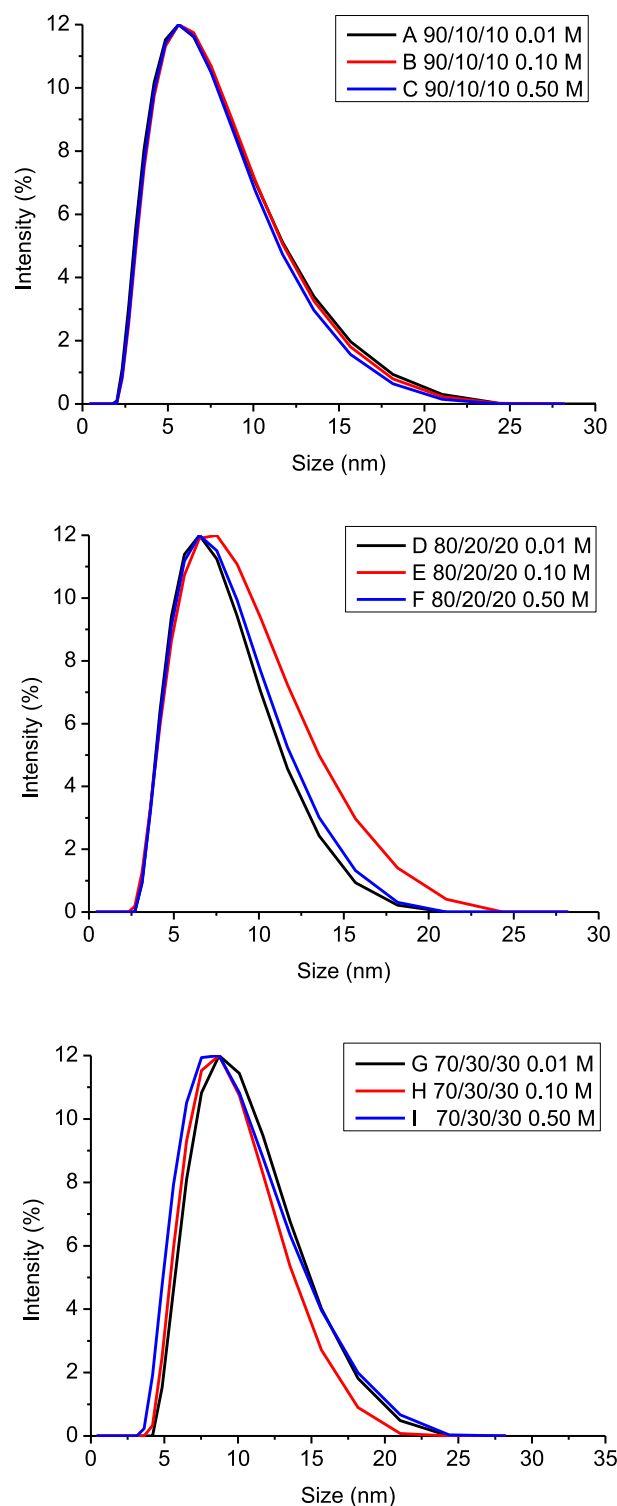


Fig. 1. DLS spectra showing particle size (nm) vs. intensity (%) for samples shown as a function of [MAPTMS/ZPO/MAAH] with three HNO_3 concentrations used for the pre-hydrolysis of MAPTMS.

size is governed by the transition metal concentration and is not affected by the pH of synthesis. However, the FWHM of the materials did vary with the lowest being observed for materials D (90/10/10, 0.01 M) and F (80/20/20, 0.50 M). All materials had a FWHM of < 8.7 nm, indicating the homogeneity of the sols. This result shows that any difference in the anticorrosion performances would be only ascribable to variations in the structure of the materials due to the different acid catalyst and ZPO

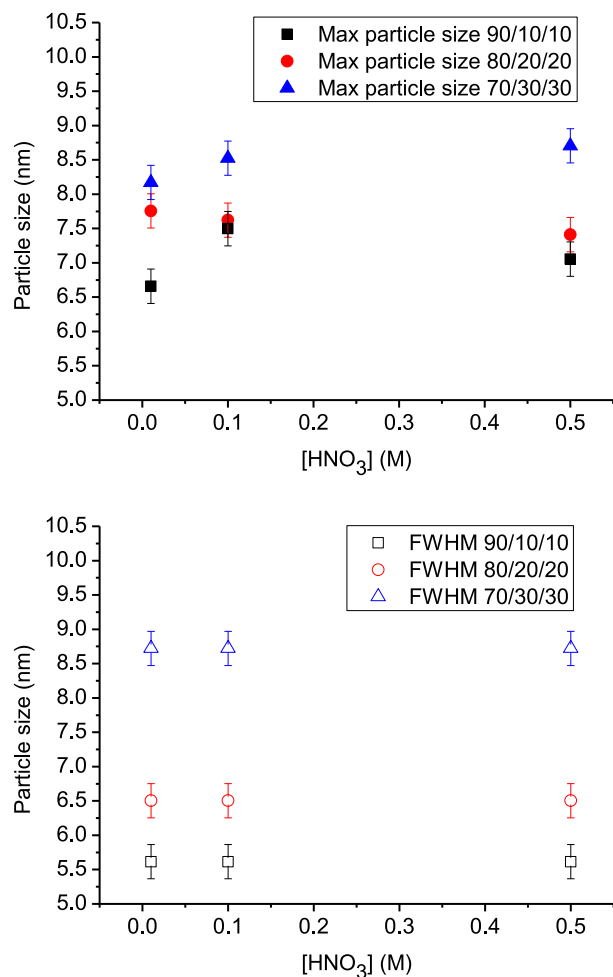


Fig. 2. Maximum particle size and FWHM of the distribution for samples prepared with three different MAPTMS/ZPO/MAAH proportions as a function of the HNO₃ concentration (M) used for the pre-hydrolysis of MAPTMS.

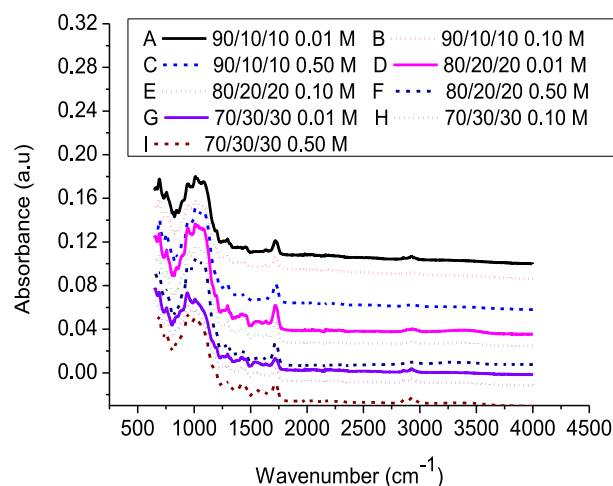


Fig. 3. FTIR spectra for samples prepared with three different MAPTMS/ZPO/MAAH proportions and three different HNO₃ concentrations used for the pre-hydrolysis of MAPTMS.

concentrations of the materials.

3.2. FTIR Analysis

As all materials were prepared with the same precursors, the FTIR spectra are found to be similar (Fig. 3). In order to identify the effect of the variables (pH and zirconium content) on the hydrolysis and

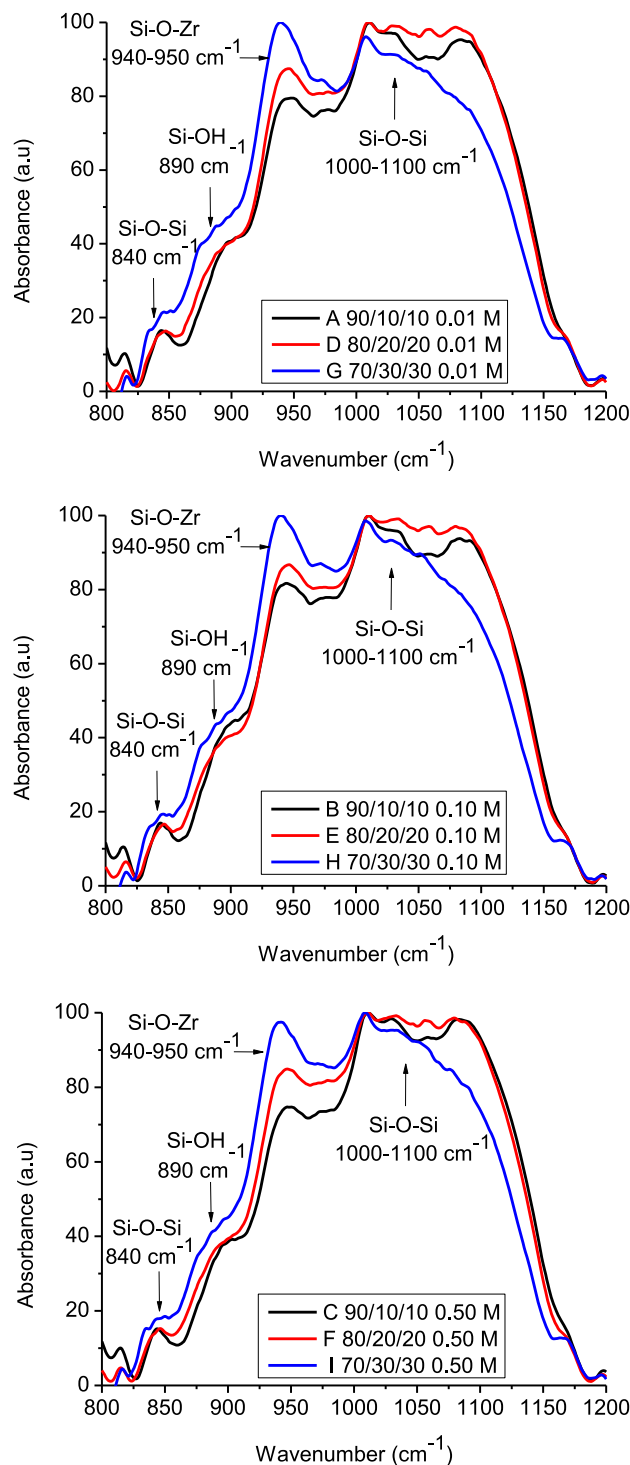


Fig. 4. FTIR spectra in the range 800-1200 cm⁻¹ for samples prepared with three different MAPTMS/ZPO/MAAH proportions as a function of the HNO₃ concentration (M) used for the pre-hydrolysis of MAPTMS, 0.01, 0.10 and 0.50 M, respectively.

condensations processes, a greater focus on the siloxane (Si-O-Si) and silicon-zirconium oxide (Si-O-Zr) has been performed, as shown in Figs. 4 and 5.

The broad band located in the range 800–1100 cm^{-1} results from the superimposition of the Si-O-Si (ν_s and ν_{as} at 840 cm^{-1} and 1000–1100 cm^{-1} , respectively), Si-O-Zr (ν_s 940–950 cm^{-1}) and Si-OH (ν_s 890 cm^{-1}) stretching vibrations. The methoxysilane symmetric vibrations

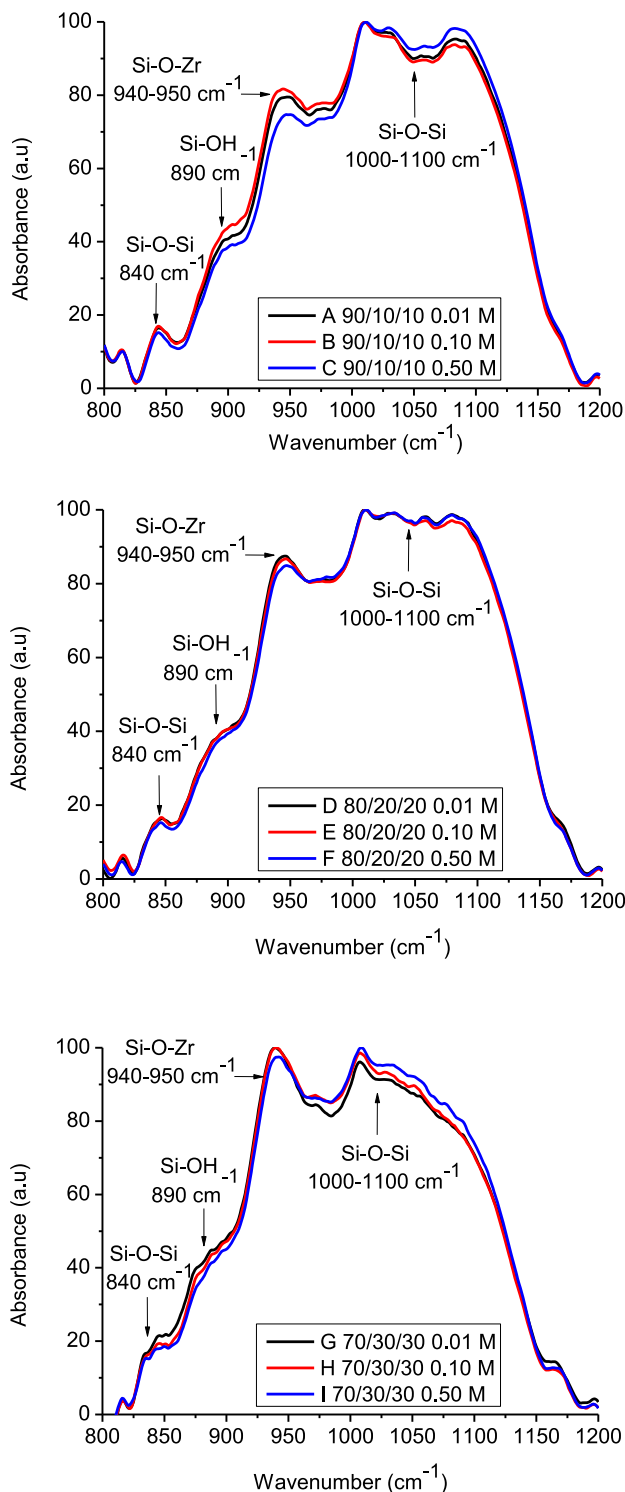


Fig. 5. FTIR spectra in the range 800–1200 cm^{-1} shown as a function of [MAPTMS/ZPO/MAAH] with three different HNO_3 concentrations used for the pre-hydrolysis of MAPTMS.

contained in the MAPTMS are located at 1170 cm^{-1} . While the bands located in the 1000–1100 cm^{-1} spectral range represent the siloxanes bonds, where in this region four bands can be distinguished at 1010, 1030, 1055 and 1080 cm^{-1} and are described in detail in previous work [9, 17]. Focusing on Fig. 4 where the materials are shown as a function of $[\text{HNO}_3]$ (0.01 M, 0.10 M and 0.50 M, respectively) and the variable being the concentration of the ZPO complex. It is evident that regardless of the pH that as the zirconium concentration is increased, there is an increase in the band at 940–950 cm^{-1} , which symbolises the Si-O-Zr groups. Interestingly, the band located at 1010 cm^{-1} , which is representative of low-energy siloxane bonds, is the same for the 10 and 20 % ZPO systems regardless of pH, however when the zirconium complex concentration is increased to 30 %, there is an observed decrease in this band. This shows that up to 20 % of ZPO complex there is still the formation of these low energy siloxane bonds, however above this the competition from the increased zirconium concentration is preferentially forming Si-O-Zr bonds. This is also evident when focusing on the other siloxane bands, located at 1030, 1055 and 1080 cm^{-1} , which are progressively decreasing, with an increase in ZPO concentration for the benefit of the band at 940–950 cm^{-1} , with the highest energy siloxane band at 1080 cm^{-1} showing the largest decrease. This indicates that the formation of Si-O-Zr groups is favoured over the formation of high-energy Si-O-Si groups.

To study the effect of the pH on the hydrolysis and condensation reactions, Fig. 5 shows series 1, 2 and 3, which only vary by pH and the zirconium concentrations, 10, 20 and 30 %, respectively, are kept constant within each series. In series 1 it can be seen that as the pH is decreased, the band located at 940–950 cm^{-1} decreases for the benefit of the high energy siloxane bands. It is evident that the low-energy siloxane bonds are formed regardless of pH and the difference is observed in the bonds that require higher energy to form, in particular the siloxane bonds which require the highest energy, located at 1080 cm^{-1} . This shows that, a more acidic environment enhances the formation of more highly condensed siloxane bonds while decreasing the formation of the Si-O-Zr bonds. This same effect is observed when a 20 % zirconium complex is employed in series 2, although slightly less pronounced. However, when the concentration of the ZPO is increased to 30 % in series 3, the decrease in the band at 940–950 cm^{-1} is still observed but primarily for the benefit of the formation of the low energy siloxane bonds located at 1030 cm^{-1} . The fact that the formation of the higher energy siloxane bonds is decreased in comparison with other materials is probably due to the steric hindrance brought about by the zirconium atom, where the condensation of Si-O-Zr bonds is favoured.

In summary, the formation of the silicate and silicate-zirconate groups can be controlled by both the concentration of the ZPO and the pH of catalysis. When the ZPO concentration is no higher than 20 % the formation of siloxane bonds can be increased by decreasing the pH and more particularly the formation of the more highly condensed siloxane bonds can be achieved. However, when the concentration of the ZPO is increased to 30 % there is a higher competition in the formation of Si-O-Zr bonds and regardless of the pH they are preferentially formed over the higher condensed Si-O-Si bonds. However, it is possible to control the formation of the lower condensed Si-O-Si bonds and this was shown with an increase in the band located at 1010 cm^{-1} with a decrease in pH.

3.3. ^{29}Si -NMR Analysis

In order to understand the influence the pH has on the hydrolysis and condensation reactions of the ormosils, ^{29}Si -NMR spectra were recorded at three different time points during the synthesis. The first was straight after the catalysed pre-hydrolysis of MAPTMS with varying HNO_3 concentrations, ‘Solution A’, secondly after the pre-hydrolysed MAPTMS and ZPO complex were mixed, ‘Solution C’, and lastly after 24 hours ageing, ‘Sol-Gel’. The ^{29}Si -NMR spectra of the pre-hydrolysed MAPTMS with 0.01, 0.10 and 0.50 M HNO_3 are shown in Fig. 6 and the % T species present are shown in Fig. 7. When a HNO_3 concentration of 0.01 M was

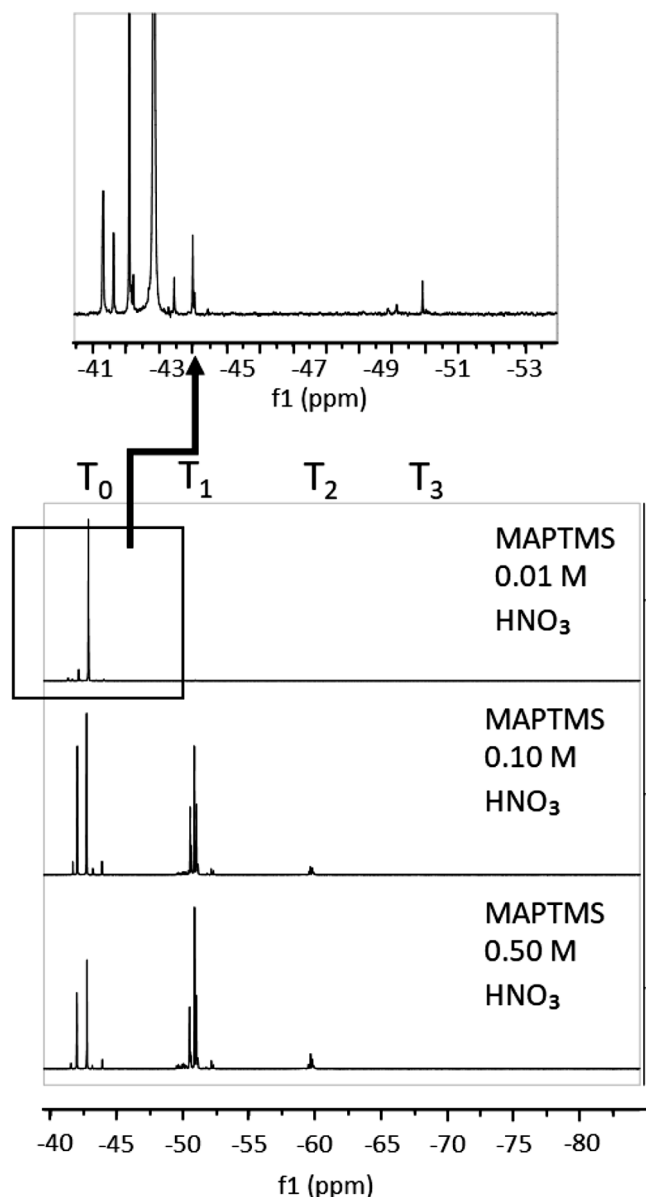


Fig. 6. Liquid state ^{29}Si -NMR spectra of pre-hydrolysed MAPTMS with 0.01, 0.10 and 0.50 M HNO_3 .

utilised, only peaks in the T_0 chemical shift range were observed. Pure un-hydrolysed MAPTMS exhibits one single sharp peak at -42.8 ppm, however there are more peaks visible within this region, located at -41.2, -41.6, -42.1, -43.5 and -44.0 ppm. Indeed, the annotation T_0 indicates that there are no oxo bridges formed between the two inorganic centres, however there are variations of T_0 groups which can be formed based on the number of hydroxyl or methoxy groups attached. The substitution of a methoxy group by a hydroxyl group induces a conventional down-field shift [18] and the shifts observed downfield have been assigned accordingly and are shown below in Table 2. However, there are two shifts observed up-field from the pure MAPTMS precursor, located at -43.5 and -44.0 ppm. These two peaks still correspond to the structure $\text{RSi}(\text{OMe})_3$, which is unreacted, though they are more than likely within different configurations. In fact, it was seen that there is a very small concentration of T_1 species forming at this stage of the synthesis and the most plausible explanation would be that these unreacted groups are entrapped within these growing T_1 nanoparticles and hence have higher electron densities and are appearing up-field.

When the concentration of the acid catalyst is increased to 0.10 M

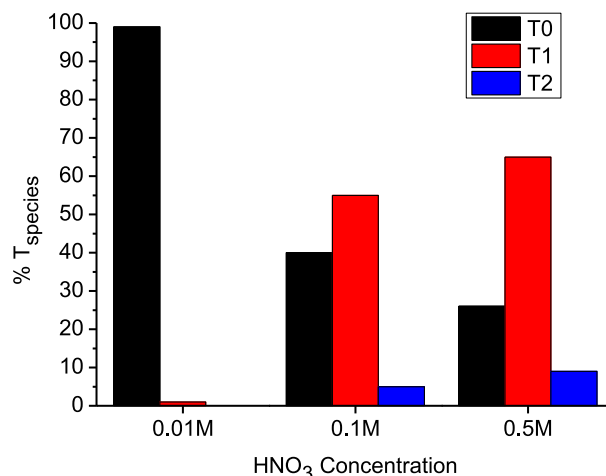


Fig. 7. % T_{species} present in pre-hydrolysed MAPTMS with 0.01, 0.10 and 0.50 M HNO_3 , as calculated from ^{29}Si -NMR spectra shown in Fig. 6.

Table 2

^{29}Si -NMR signals for monomeric species obtained from the MAPTMS hydrolysis reactions

Structure	Notation	Chemical shift (ppm) ± 0.1 ppm
$\text{RSi}(\text{OMe})_3$	T_0^0	-42.8
$\text{RSi}(\text{OMe})_2\text{OH}$	T_1^0	-42.1
$\text{RSiOMe}(\text{OH})_2$	T_2^0	-41.6
$\text{RSi}(\text{OH})_3$	T_3^0	-41.2

there are both T_1 and T_2 species formed in relative concentrations of 55 and 5 %, respectively. When the concentration of HNO_3 is further increased to 0.50 M there is an observed increase in the hydrolysis and hence the condensation reactions of the Si related moieties and T_1 and T_2 species are present in concentrations of 65 and 9 %. Hence, this is direct proof that the increase in the concentration of the acid catalyst increases the kinetics of reaction, resulting in higher concentrations of both hydrolysed and condensed silicate species.

The ^{29}Si -NMR spectra of 'Solution C' for all materials are shown below in Fig. 8. To quantify the content of the different silicate species for each material, the signals were integrated and the relative % T_{species} present in each material are shown in Fig. 9. It can be seen that in all materials there are no T_3 species formed at this stage of the synthesis regardless of the pH or transition metal concentration utilised. However, there are differences observed in the relative concentrations of the T_0 , T_1 and T_2 species. In all series, regardless of the concentration of the transition metal complex it can be seen that as the pH is decreased to a more acidic environment there is an observed increase in concentration of both the T_1 and T_2 species to the detriment to the uncondensed T_0 species. The same pattern is observed in all series where a decrease of 27, 27 and 41 % is seen in the T_0 species as the HNO_3 concentration is increased from 0.01 to 0.50 M in series 1, 2 and 3, respectively. It is well known that acid catalysed sol-gel reactions speed up the hydrolysis of the silanol groups, hence provoking the condensation of the siloxane bonds, thus confirming the FTIR results.

Given differences were observed throughout the synthesis in the hydrolysis and condensation reactions it was important to determine whether the pH had an effect on the materials after 24 hours ageing, when the sols are deposited on the Al alloy. Therefore, the ^{29}Si -NMR spectra were also recorded at this time and are shown in Fig. 10. In order to quantify the relative concentrations of the different silicate species, the signals were integrated and are shown as a percentage of T_{species} in Fig. 11. It can be seen in all materials that there are no T_0 and T_1 species remaining and only T_2 and T_3 species are present. This indicates the

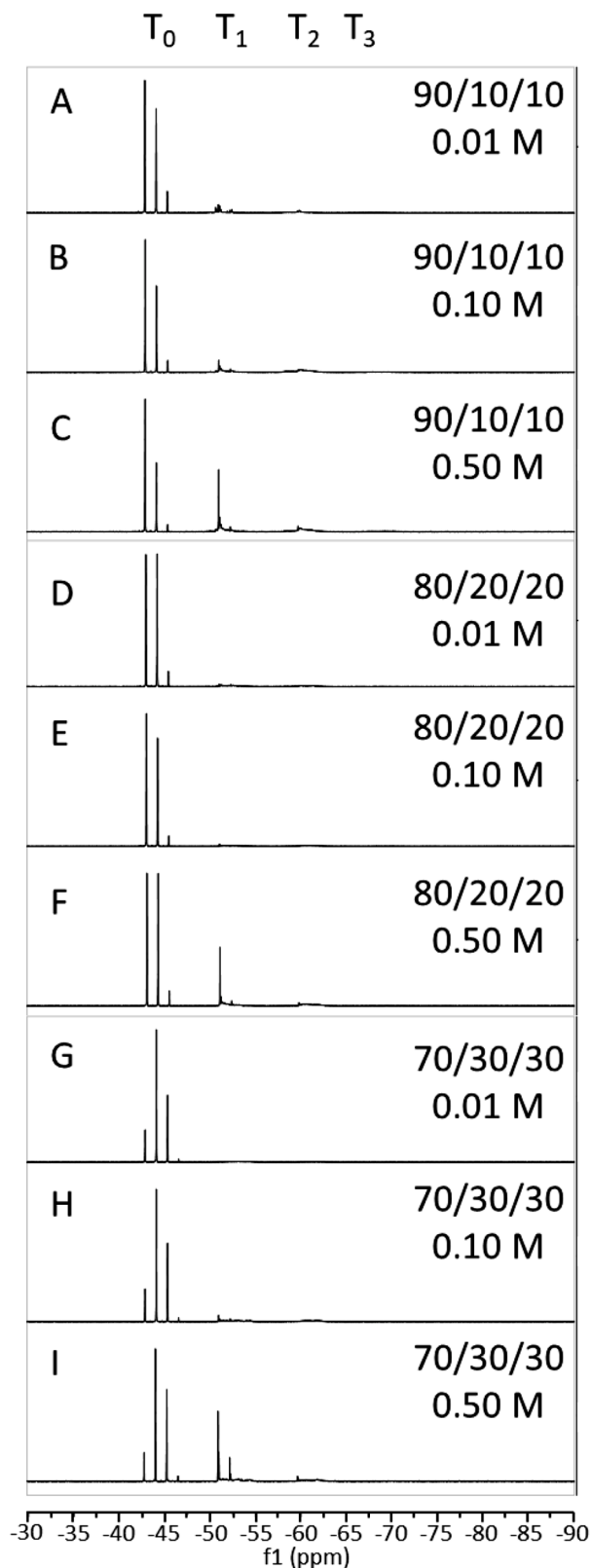


Fig. 8. Liquid state ^{29}Si -NMR spectra of all samples shown as a function of [MAPTMS/ZPO/MAAH] with three different HNO₃ concentrations used for the pre-hydrolysis of MAPTMS, after mixing of MAPTMS with ZPO.

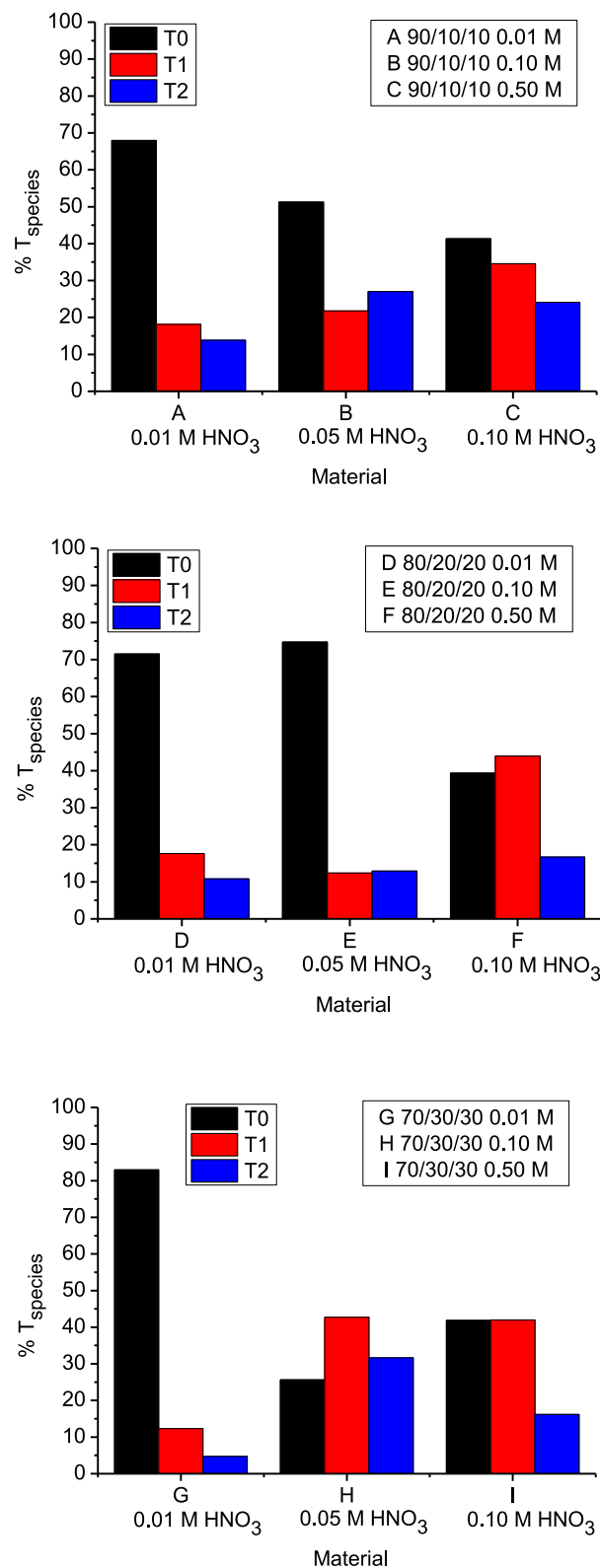


Fig. 9. % T₀ species present in all samples shown as a function of [MAPTMS/ZPO/MAAH] with three different HNO₃ concentrations (M) used for the pre-hydrolysis of MAPTMS, after mixing of MAPTMS with ZPO, as calculated from ^{29}Si -NMR spectra shown in Fig. 8.

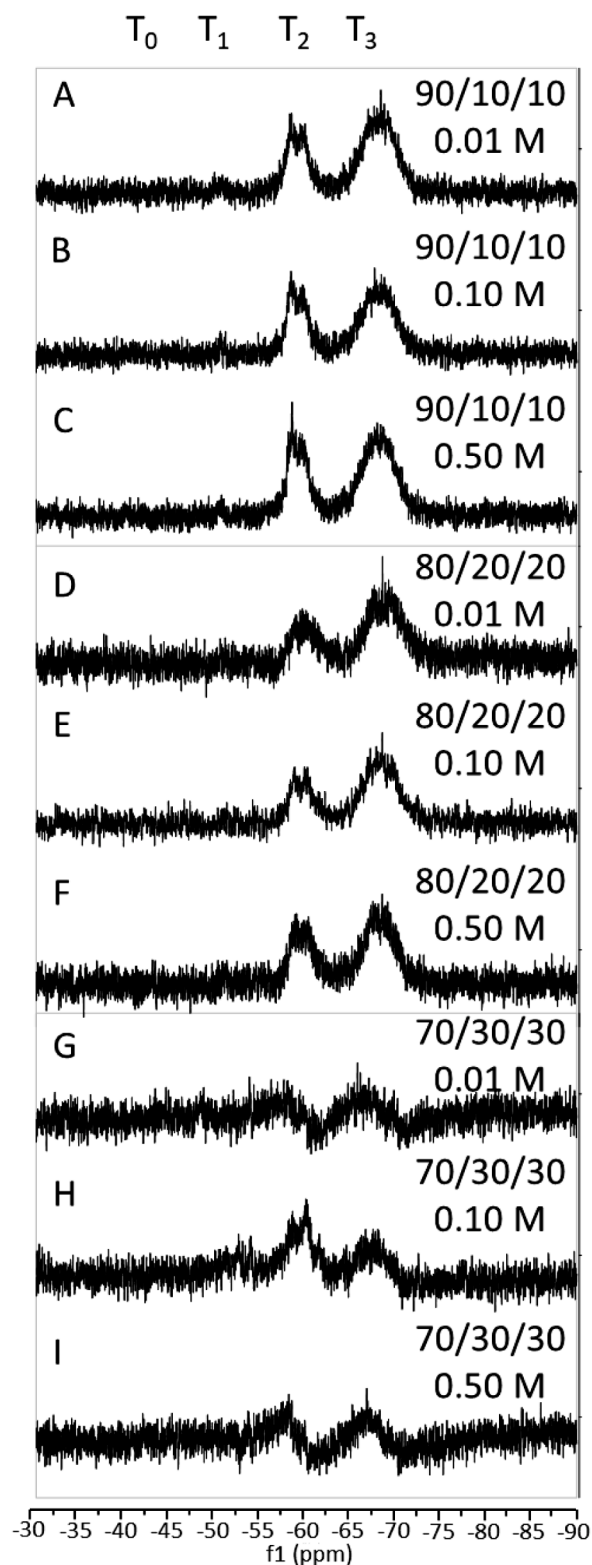


Fig. 10. Liquid state ^{29}Si -NMR spectra of all samples shown as a function of [MAPTMS/ZPO/MAAH] with three different HNO_3 concentrations (M) used for the pre-hydrolysis of MAPTMS, after 24 hours ageing.

condensation of the silicate network has taken place, thus explaining the difference in the signal to noise ratio (SNR) of the spectra in comparison with those recorded in Fig 8. Indeed, SNR are primarily due to the difference in the condensation of the materials, which increase the anisotropic character, thus the disorder of the electronic distribution around

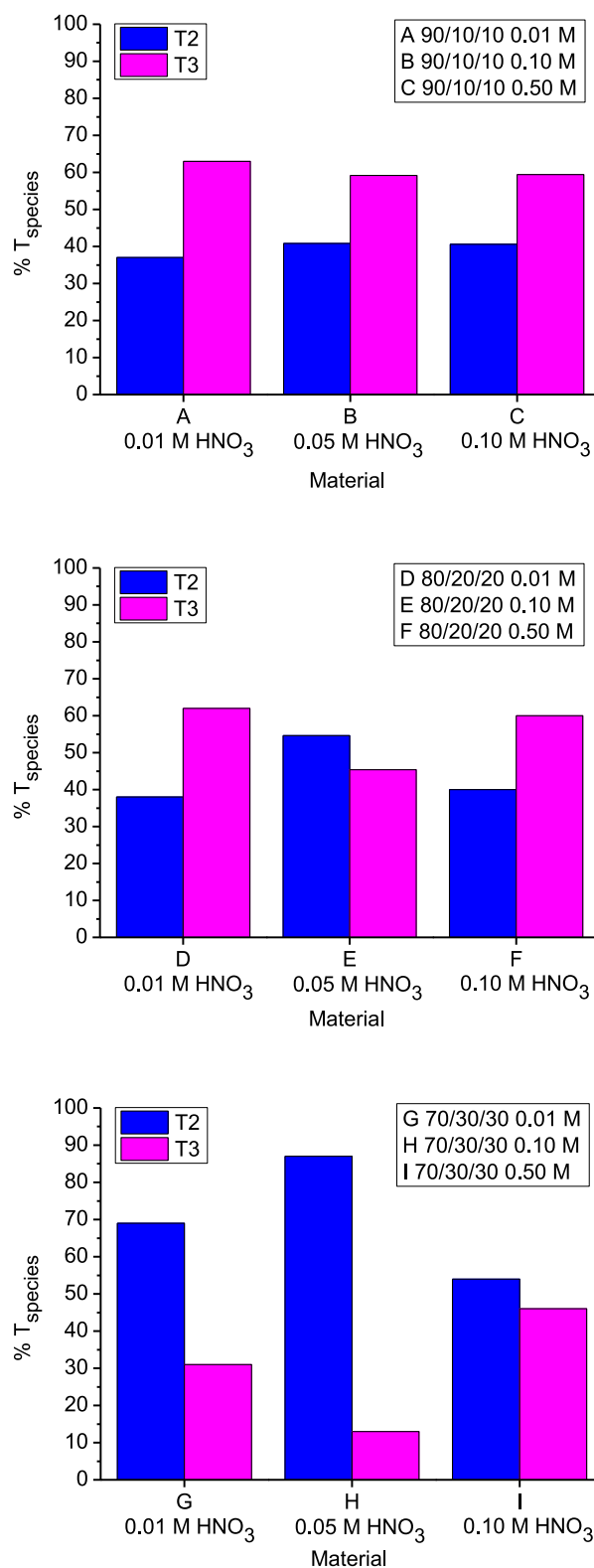


Fig. 11. % Tspecies present in all samples shown as a function of [MAPTMS/ZPO/MAAH] with three different HNO_3 concentrations used for the pre-hydrolysis of MAPTMS, after 24 hours ageing, as calculated from ^{29}Si -NMR spectra shown in Fig. 10.

silicon nuclei with respect to the external magnetic field [19]. Series 1 exhibited the highest amount of T_3 species with concentrations of 63, 59 and 60 % for materials A, B and C, respectively. The concentration of T_3 species in series 2 was 62, 45 and 60 % for materials D, E and F,

respectively, while series 3 had concentrations of 31, 13 and 46 for materials G, H and I, respectively. The progressive decrease in the % of T₃ species formed from series 1 to series 3 may be due to the steric hindrance of the zirconium atom, reducing interaction between the silicate species. This confirms the FTIR results, as it was observed that when the zirconium concentration was increased, the formation of the siloxane bonds was seen to decrease for the benefit of the Si-O-Zr bonds.

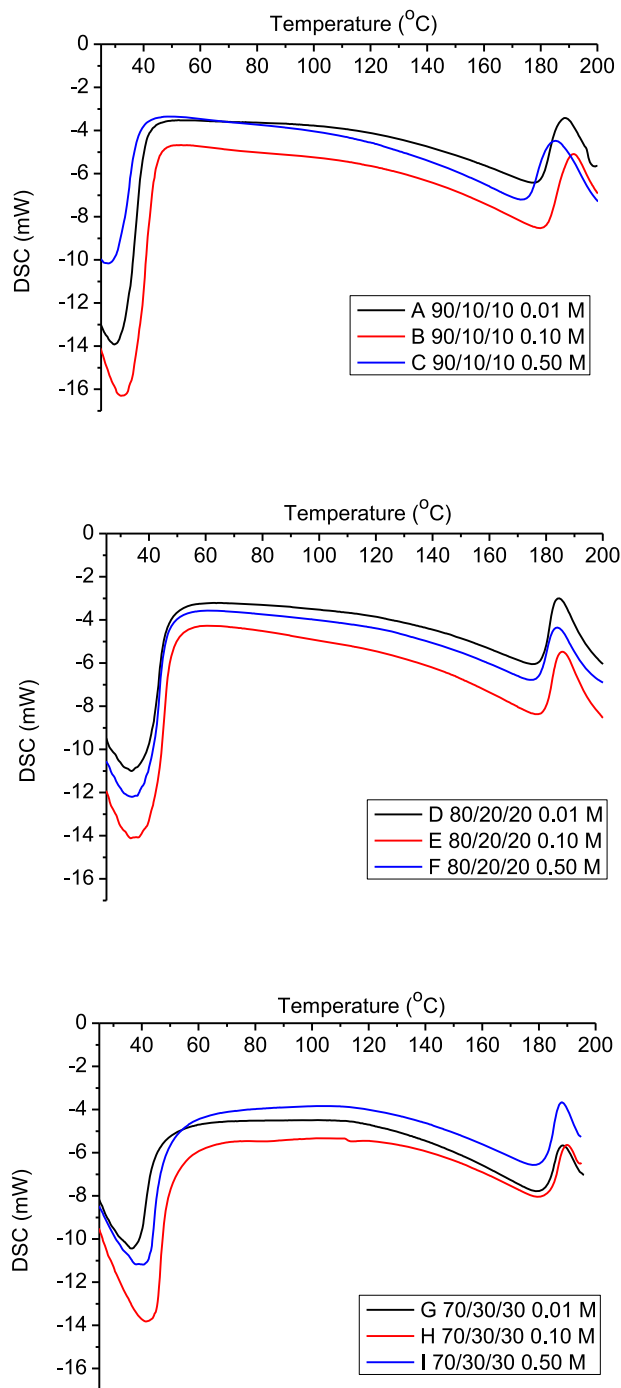


Fig. 12. DSC curves of samples after 24 hours ageing from three different MAPTMS/ZPO/MAAH proportions in the precursor solution as a function of the HNO₃ concentration (M) used for the pre-hydrolysis of MAPTMS.

3.4. DSC Analysis

DSC analysis was performed on liquid sol-gel materials between room temperature and 200°C. Fig. 12 shows the DSC spectra recorded for all materials in series 1, 2 and 3, respectively. In these spectra, three different thermal zones can be identified namely, below 100°C, between 100 and 150°C and above 150°C, where typically the evaporation of the solvents, condensation reactions and glass transition take place, respectively. The endothermic band observed below 60°C is characteristic of the solvent evaporation formed during the hydrolysis and condensation reactions as well as contained in the precursors. In all series it was observed that the materials prepared with 0.10 M HNO₃ (B, E and H) presented the largest endothermic band, indicating the largest amount of solvent entrapment in these systems when compared to the 0.01 M and 0.50 M prepared materials. There is a negative slope observed between 100 and 150°C for all materials; however, the extent of the slope is seen to decrease with an increasing zirconium concentration, from series 1 to 3, respectively. This endothermic band is indicative of thermally catalysed condensation reactions taking place. The fact that the extent of the endothermic phenomena is decreasing with an increase in Zr concentration indicates that the zirconium has a direct effect on the condensation reactions in the liquid phase, which was further confirmed using FTIR spectroscopy. However, within each series it should be noted that the variation in the pH had little effect on the endothermic profile observed in this region. The T_g of the materials is characterised as the full solidification point of the material and it was observed that within each series there was only a variation of $\pm 1^\circ\text{C}$, indicating that the pH has no significant influence. On the other hand, when comparing the series between each other it appears that the solidification point ranges between 185 and 190°C, suggesting the zirconium content has negligible effect on the full solidification point of all materials. However, as the characteristic band of the T_g is clearly seen to narrow with the increase of the zirconium content, this demonstrates that the structures formed are more homogeneous; therefore, the zirconium having a structuring role to the silicate matrix, confirming the FTIR results.

3.5. SEM/EDX Analyses

All coatings were found to be homogeneously deposited on the aluminium alloy with coating thicknesses close to $4.6 \mu\text{m} \pm 0.2 \mu\text{m}$, as shown in the example in Fig. 13. EDX analysis of the coatings' cross-section (Fig. 14) shows a uniform distribution of the main elements contained in the sol-gel precursors (oxygen, silicon and zirconium) and the aluminium alloy seen at the bottom of the image. The uniform distribution of all chemical species within the coating demonstrates the homogeneity of the materials prepared.

3.6. EIS

The anticorrosion properties of the coatings on AA2024-T3 alloys were characterised using EIS. The bode plots were recorded for all coatings at 24-hour increments for 192 hours and a selection of 0, 72, and 192 hours are displayed in Fig. 15. At 0 hours exposure, one time

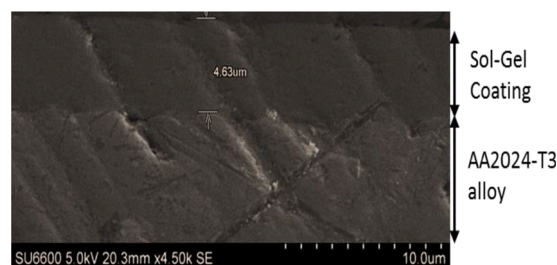


Fig. 13. SEM image of coating E (80/20/20 0.10 M HNO₃).

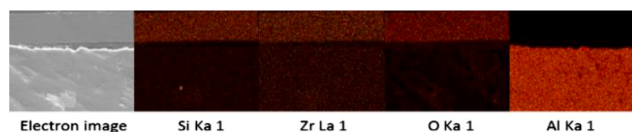


Fig. 14. EDX analysis of coating E (80/20/20 0.10 M HNO_3).

constant can be distinguished at high frequency for all materials, while materials C, D, E, G and I all exhibit a second time constant in the middle frequency range, indicating the early penetration of the electrolyte through the coatings and perhaps the oxidation of the surface of the metal substrate. All materials exhibit similarities in terms of phase differences between 0-, 72-, and 192-hours exposure time, with an observed shift towards lower frequencies for all materials, suggesting the occurrence of the corrosion process.

In order to highlight the performances of the coating's series within the exposure times, the evolutions of the impedance at 10^{-2} Hz for all coatings are displayed in Fig. 16. This representation provides indications on the overall corrosion resistances of the coatings as well as

the short- and long-term resistances. It can be seen for all coatings that this value decreases as a function of exposure time. Indeed, at 0 hours exposure all coatings had impedance values ranging between $10^{6.6}$ and $10^{7.7} \Omega \text{ cm}^2$, with series 1 dominating the two other series, thus showing a better short-term corrosion resistance. However, in order to identify the long-term corrosion resistance within each series and within all series, the evolution of % impedance at 10^{-2} Hz over 192 hours exposure would be more representative than the absolute value of the impedance, as represented in Fig. 17. It can be seen that within each series the effect of the pH is provoking different behaviours. Indeed, for series 1, the decrease of the pH enables to reduce the % of impedance. For series 2, it appears that the pH of 1 would provide the least percentage decrease of the impedance (material E), while for series 3, the decrease of the pH has an opposite effect by progressively increasing the variation of the impedance. This indicates the effect of the pH is strongly related to the concentrations of zirconium, thus to the structure of the material. When comparing the three series to each other it appears that material G with a 25 % decrease of its initial impedance would be the coating exhibiting the highest long-term corrosion resistance. This may be due to the best

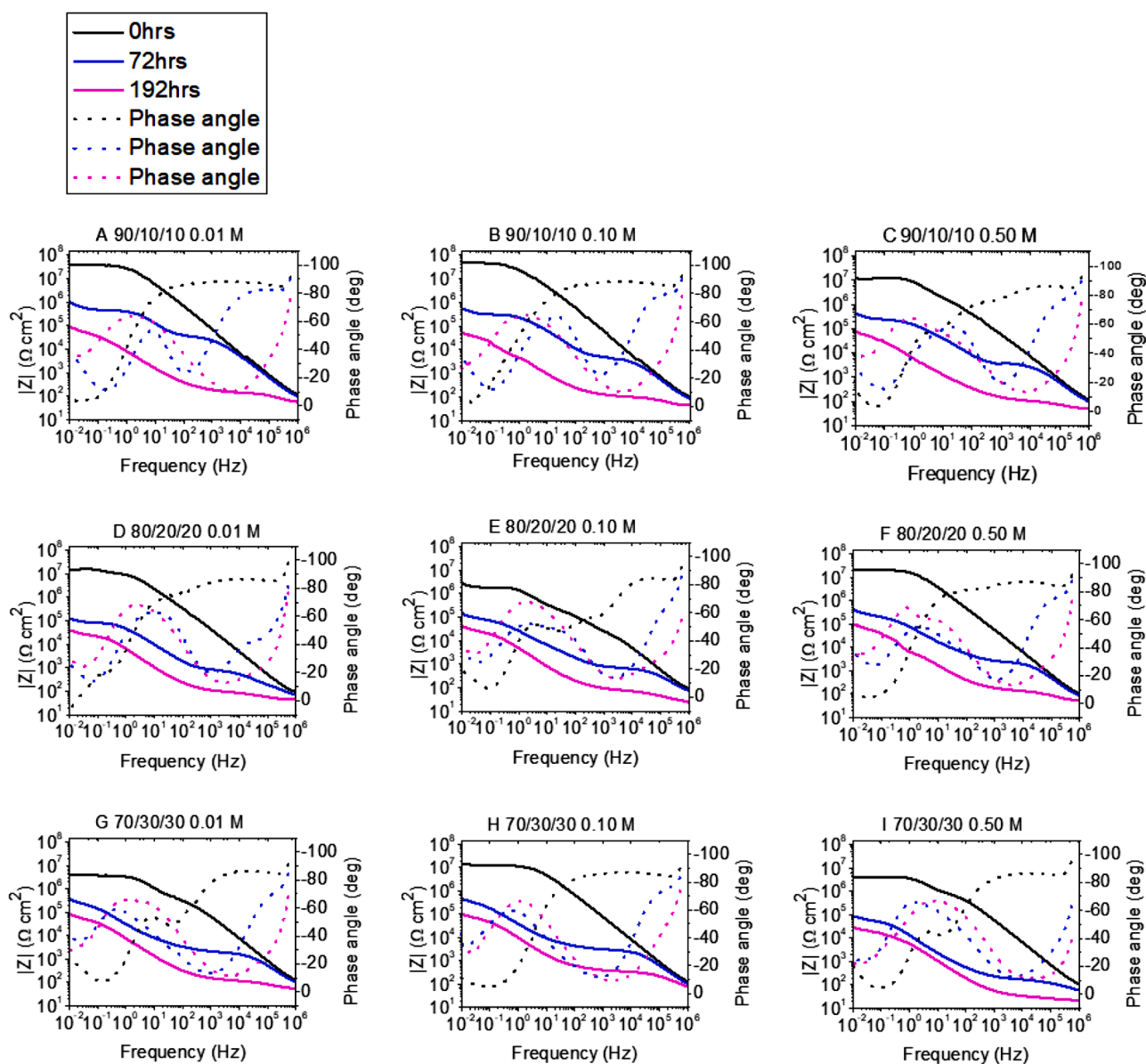


Fig. 15. Bode plots of coatings after 0-, 72-, and 192-hours of immersion in a 3.5 wt. % NaCl solution for materials prepared with different MAPTMS/ZPO/MAAH proportions in the precursor solution as a function of the HNO_3 concentration (M) used for the pre-hydrolysis of MAPTMS.

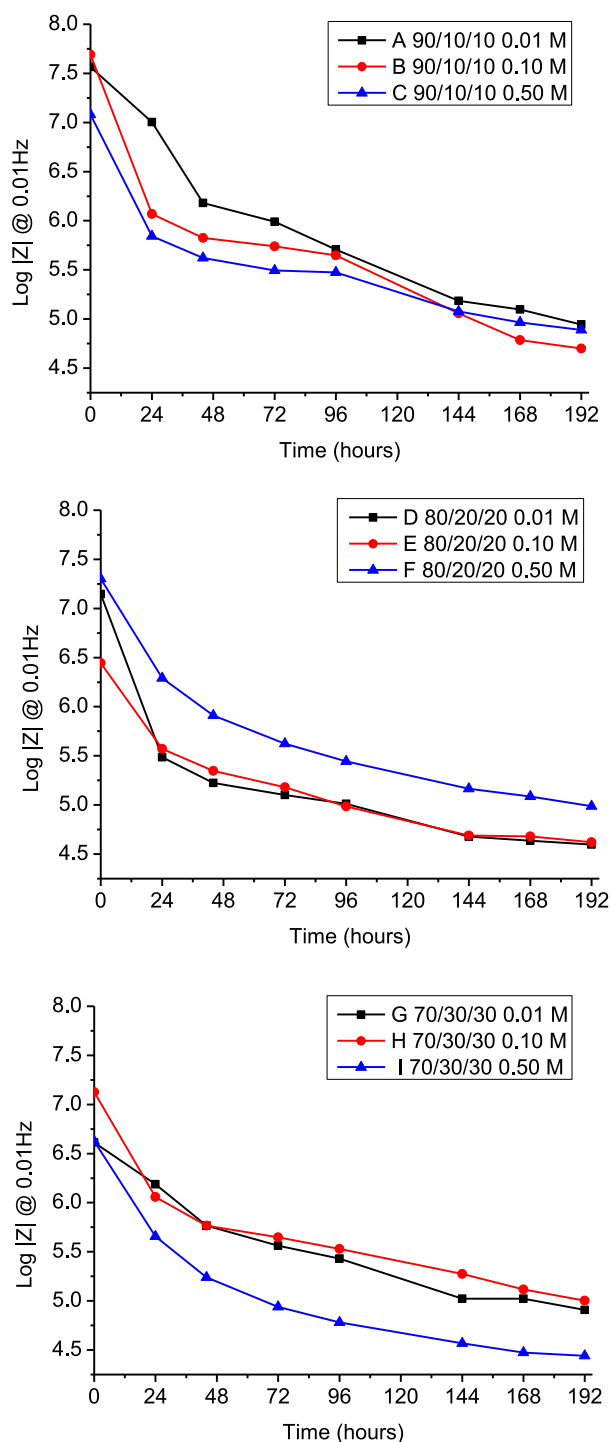


Fig. 16. Representation of the evolution of the impedance at frequency 10–2 Hz over 192 hours for materials prepared with different MAPTMS/ZPO/MAAH proportions in the precursor solution as a function of the HNO₃ concentration (M) used for the pre-hydrolysis of MAPTMS.

compromise between the sol-gel synthesis and the structure of the hybrid network.

3.7. NSS

NSS was operated according to ISO 9227. The samples were examined every 24 hours of exposure to salt spray fog for 216 hours and a selection of images at 24, 72, 120 and 216 hours are shown in Fig. 18. To quantify the corrosion resistance of the coatings, the number of pits per

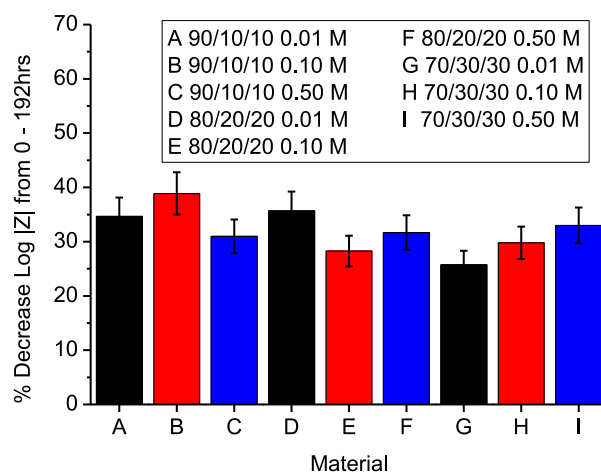


Fig. 17. Percentage decrease of impedance from 0–192 hours immersion for materials prepared with different MAPTMS/ZPO/MAAH proportions in the precursor solution as a function of the HNO₃ concentration used for the pre-hydrolysis of MAPTMS.

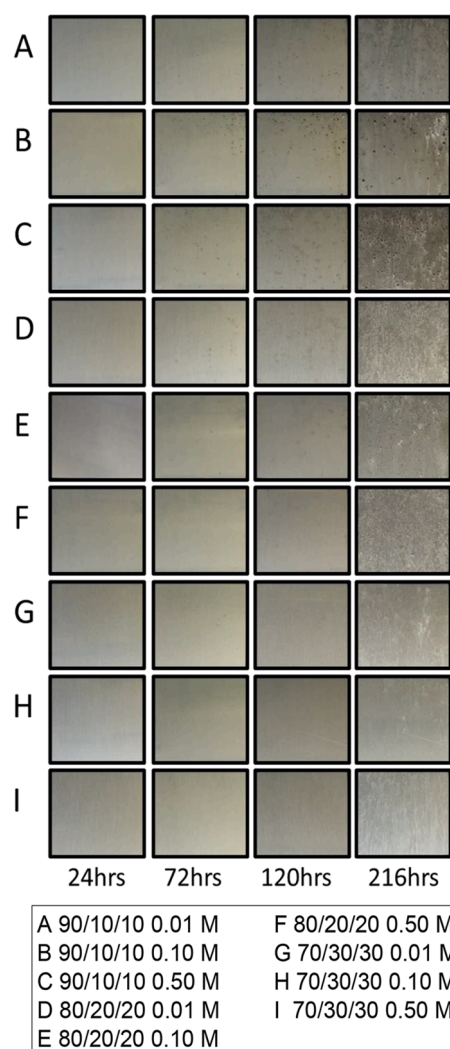


Fig. 18. Images of coatings prepared with different MAPTMS/ZPO/MAAH proportions in the precursor solution as a function of the HNO₃ concentration used for the pre-hydrolysis of MAPTMS after 24-, 72-, 120-, and 216-hours exposure to NSS.

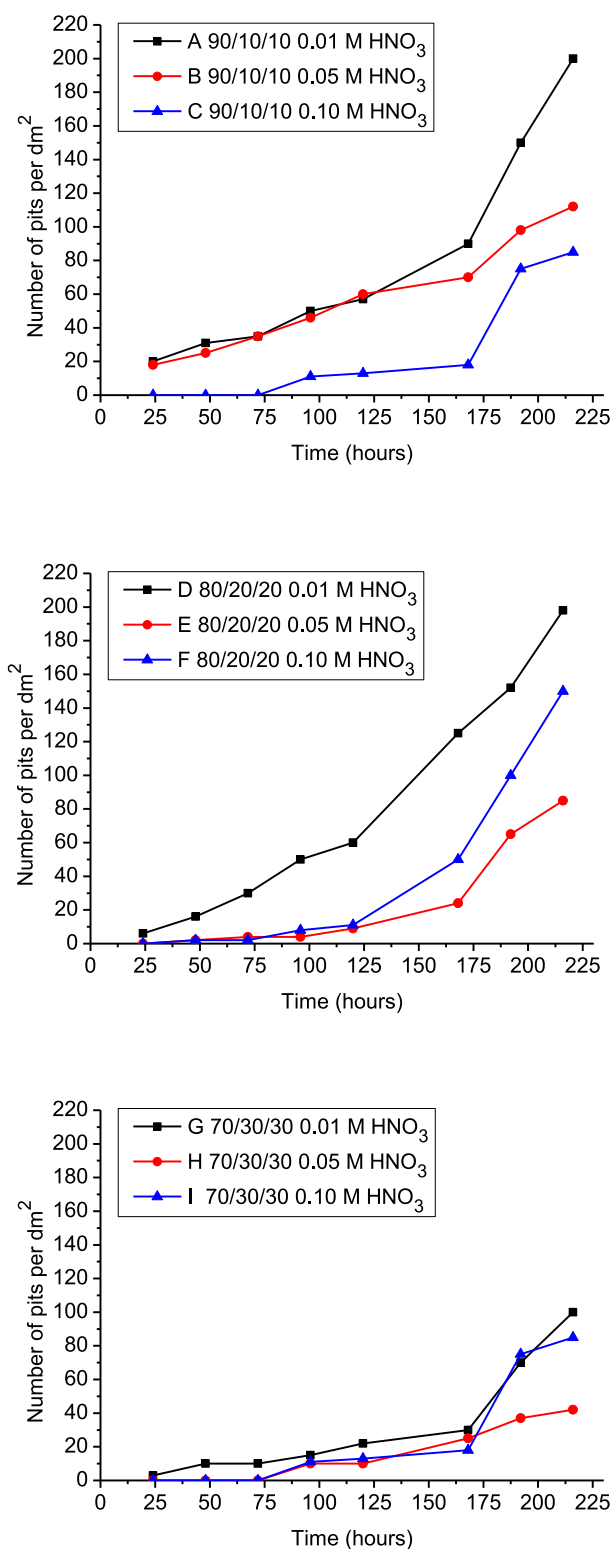


Fig. 19. Number of pits per dm^2 from 0 – 216 hours of NSS exposure for coatings prepared with different MAPTMS/ZPO/MAAH proportions in the precursor solution as a function of the HNO_3 concentration used for the pre-hydrolysis of MAPTMS.

dm^2 as a function of exposure time for each coating is presented in Fig. 19. After 24 hours of exposure, series 1 all presented signs of corrosion with pits of 20, 18 and 10 observed for materials A-C, respectively. At the same time, series 2 and 3 all presented less than 3

pits per dm^2 , with coatings F, H and I showing none. From 24 to 216 hours of exposure, all coatings showed an increase in the number of pits per dm^2 , the lowest increase is observed for materials E, G, H and I. Importantly, unlike all other coatings, coating H showed the least number of pits with no further increase from 192 to 216 hours, suggesting a better long-term corrosion resistance than all other materials developed here. Similar to the results obtained by EIS, these results show that the materials with zirconium content of 20 and 30 % exhibit a higher corrosion resistance than those containing 10 % and that the pH has an active role on the corrosion resistance. However, although EIS and NSS have resulted in different optimum materials (G and H, respectively), probably due to the techniques themselves, they have highlighted the materials that showed the highest interconnectivity between the silicate and the zirconium complex, namely the highest content of Si-O-Zr bonds as identified by FTIR and ^{29}Si -NMR analyses. It is likely that this would result in materials with greater density, thus acting as more efficient barriers against corrosion in an alkaline environment.

4. Conclusion

The aim of this work was to identify the effect the catalyst pH had on the hydrolysis and condensation reactions of the hybrid sol-gel and its subsequent effects on the anticorrosion performances of the final coatings. The FTIR analysis showed that the formation of siloxane and Si-O-Zr bonds within the network can be adjusted depending on the pH of the catalyst used and the zirconium content. Indeed, for 10 and 20 % zirconium contents, when the pH was lowered, the relative concentrations of siloxane bonds were increased at the expenses of the Si-O-Zr bonds. When the concentration of zirconium is increased to 30 %, there is a higher competition in the formation of Si-O-Zr bonds and they are preferentially formed over the higher condensed Si-O-Si bonds as the pH is increased. These results were supported by ^{29}Si -NMR characterisations, confirming that the interconnectivity between the silicate and zirconium was favoured in a less acidic environment, when the content of zirconium was fixed at 30 %. The corrosion studies shed light on the effects of these structural characteristics on the anticorrosion performances of the coatings. Indeed, it was found that the materials that contained the highest concentration of Si-O-Zr bonds exhibited the highest long-term corrosion resistance in an alkaline environment, due to the increase in interconnectivity between the two material systems, resulting probably in more condensed coatings.

Declaration Of Competing Interest

The authors declare that they have no known competing financial interests or personal relationships that could have appeared to influence the work reported in this paper.

The authors declare the following financial interests/personal relationships which may be considered as potential competing interests:

References

- [1] TK, Shruthi, J. Walton, S. McFall-Boegeman, S. Westre, GM Swain, Investigation of the Trivalent Chromium Process Conversion Coating as a Sealant for Anodized AA2024-T3, 2020. J. Electrochem. Soc. 111504. doi:10.1149/1945-7111/aba4ea.
- [2] R. Berger, U. Bexell, T. Mikael Grehk, S.E. Hörnström, A comparative study of the corrosion protective properties of chromium and chromium free passivation methods, Surf. Coat. Technol. 202 (2007) 391–397, <https://doi.org/10.1016/j.surfcoat.2007.06.001>.
- [3] M.A. Hafeez, A. Farooq, A. Zang, A. Saleem, K.M. Deen, Phosphate chemical conversion coatings for magnesium alloys: a review, J. Coat. Technol. Res 17 (2020) 827–849, <https://doi.org/10.1007/s11998-020-00335-2>.
- [4] P. Campestrini, H. Terryn, A. Hovestad, J.H.W. De Wit, Formation of a cerium-based conversion coating on AA2024 : relationship with the microstructure, Surf. Coat. Technol. 176 (2004) 365–381, [https://doi.org/10.1016/S0257-8972\(03\)00743-6](https://doi.org/10.1016/S0257-8972(03)00743-6).
- [5] W.G. Fahrenholtz, M.J. O'Keefe, H. Zhou, J.T. Grant, Characterization of cerium-based conversion coatings for corrosion protection of aluminum alloys, Surf. Coat. Technol. 155 (2002) 208–213, [https://doi.org/10.1016/S0257-8972\(02\)00062-2](https://doi.org/10.1016/S0257-8972(02)00062-2).

- [6] H. Guan, R.G. Buchheit, Corrosion protection of aluminum alloy 2024-T3 by vanadate conversion coatings, *Corrosion* 60 (2004) 284–296, <https://doi.org/10.5006/1.3287733>.
- [7] R.B. Figueira, C.J.R. Silva, E.V. Pereira, Organic–inorganic hybrid sol–gel coatings for metal corrosion protection: a review of recent progress, *J. Coat. Technol. Res* 12 (2015) 1–35, <https://doi.org/10.1007/s11998-014-9595-6>.
- [8] Rodič Peter, Maria Lekka, Francesco Andreatta, Lorenzo Fedrizzi, Ingrid Milošev, The effect of copolymerisation on the performance of acrylate-based hybrid sol-gel coating for corrosion protection of AA2024-T3, *Prog. Org. Coat* 147 (2020), 105701, <https://doi.org/10.1016/j.porgcoat.2020.105701>.
- [9] F.X. Perrin, F. Ziarelli, A. Dupuis, Relation between the corrosion resistance and the chemical structure of hybrid sol-gel coatings with interlinked inorganic-organic network, *Prog. Org. Coat* 141 (2020), 105532, <https://doi.org/10.1016/j.porgcoat.2019.105532>.
- [10] Peter Rodič, Ingrid Milošev, Maria Lekka, Francesco Andreatta, Lorenzo Fedrizzi, Corrosion behaviour and chemical stability of transparent hybrid sol-gel coatings deposited on aluminium in acidic and alkaline solutions, *Prog. Org. Coat* 124 (2018) 286–295, <https://doi.org/10.1016/j.porgcoat.2018.02.025>.
- [11] Mohamed Oubaha, *Sol-Gel Strategies for Hybrid Materials*, World Scientific Reference of Hybrid Materials, World Scientific, Singapore (2019). ISBN 978-981-3270-55-8.
- [12] M. Cullen, M. Morshed, M. O'Sullivan, E. MacHugh, B. Duffy, M. Oubaha, Correlation between the structure and the anticorrosion barrier properties of hybrid sol-gel coatings : application to the protection of AA2024-T3 alloys, *J. Sol-Gel Sci. Technol* 82 (2017) 801–816, <https://doi.org/10.1007/s10971-017-4349-4>.
- [13] M. Cullen, M. O'Sullivan, A.M. Kumar, A.A. Sorour, B. Duffy, M. Oubaha, The role of the hydrolysis and zirconium concentration on the structure and anticorrosion performances of a hybrid silicate sol-gel coating, *J. Sol-Gel Sci. Technol* 86 (2018) 553–567, <https://doi.org/10.1007/s10971-018-4657-3>.
- [14] C.J. Brinker, Hydrolysis and Condensation of Silicates: Effects on Structure, *J. Non-Cryst. Solids* 100 (1988) 31–50, [https://doi.org/10.1016/0022-3093\(88\)90005-1](https://doi.org/10.1016/0022-3093(88)90005-1).
- [15] F.D. Osterholtz, E.R. Pohl, Kinetics of the hydrolysis and condensation of organofunctional alkoxysilanes: a review, *J. Adhes. Sci. Technol* 6 (1992) 127–149, <https://doi.org/10.1163/156856192X00106>.
- [16] M.A. Fardad, Catalysts and the structure of SiO₂ sol-gel films, *J. Mater. Sci* 35 (2000) 1835–1841, <https://doi.org/10.1023/A:1004749107134>.
- [17] L. Lerot, P.F. Low, Effect of swelling on the infrared absorption spectrum of montmorillonite, *Clays Clay Miner* 24 (1976) 191–199, <https://doi.org/10.1346/CCMN.1976.0240407>.
- [18] M. Oubaha, M. Smahi, P. Etienne, P. Coudray, Y. Moreau, Spectroscopic characterization of intrinsic losses in an organic–inorganic hybrid waveguide synthesized by the sol–gel process, *J. Non-Cryst. Solids* 318 (2003) 305–313, [https://doi.org/10.1016/S0022-3093\(02\)01889-6](https://doi.org/10.1016/S0022-3093(02)01889-6).
- [19] F. Nardelli, S. Borsacchi, L. Calucci, et al., Anisotropy and NMR spectroscopy, *Rend. Fis. Acc. Lincei* 31 (2020) 999–1010, <https://doi.org/10.1007/s12210-020-00945-3>.